Estimating functional connectivity in an electrically coupled interneuron network

Pepe Alcami[1] and Alain Marty[1]

Laboratoire de Physiologie Cérébrale, Centre National de la Recherche Scientifique and Université Paris Descartes, 75006 Paris, France

Edited by Michael V. L. Bennett, Albert Einstein College of Medicine, Bronx, NY, and approved October 23, 2013 (received for review June 18, 2013)

Even though it has been known for some time that in many mammalian brain areas interneurons are electrically coupled, a quantitative description of the network electrical connectivity and its impact on cellular passive properties is still lacking. Approaches used so far to solve this problem are limited because they do not readily distinguish junctions among direct neighbors from indirect junctions involving intermediary, multiply connected cells. In the cerebellar cortex, anatomical and functional evidence indicates electrical coupling between molecular layer interneurons (basket and stellate cells). An analysis of the capacitive currents obtained under voltage clamp in molecular layer interneurons of juvenile rats or mice reveals an exponential component with a time constant of ∼20 ms, which represents capacitive loading of neighboring cells through gap junctions. These results, taken together with dual cell recording of electrical synapses, have led us to estimate the number of direct neighbors to be ∼4 for rat basket cells and ∼1 for rat stellate cells. The weighted number of neighbors (number of neighbors, both direct and indirect, weighted with the percentage of voltage deflection at steady state) was 1.69 in basket cells and 0.23 in stellate cells. The last numbers indicate the spread of potential changes in the network and serve to estimate the contribution of gap junctions to cellular input conductance. In conclusion the present work offers effective tools to analyze the connectivity of electrically connected interneuron networks, and it indicates that in juvenile rodents, electrical communication is stronger among basket cells than among stellate cells.

In various brain regions, GABAergic interneurons (INs) are grouped in families sharing morphological and functional properties. These families are linked together with a mix of chemical and electrical synapses. The combination of IN intrinsic firing properties with the unique connectivity offered by GABAergic and electrical synapses has been suggested to promote synchrony and rhythmic activity in the IN network (1–5).

To model the functional role of gap junctions (GJs) in the IN network and in cellular computation, it is necessary to determine the number of cells that are connected to a given cell, as well as the geometry of the network. Methods that have been developed to extract this information include dye coupling analysis (e.g., ref. 6), paired recordings coupled with anatomical descriptions (7), and frequency-dependent impedance measurements (8). The first two methods do not readily distinguish direct connections from indirect connections involving an intermediate IN (7, 9, 10), and all three methods are labor intensive and difficult to implement in a fully quantitative manner. In addition, they do not provide information on the spatial arrangement of the GJs. Therefore, the data that have been exploited for modeling GJ connectivity in IN networks are missing critical elements.

In the cerebellum, Golgi cells and molecular layer interneurons (MLIs) have been shown to form anatomical and functional networks involving GJs that are specific to a given cell type (6, 11–14). In both cases GJs may be involved in the generation of concerted oscillations under some pharmacological conditions (12, 15), and spikelets (spikes of coupled cells filtered through GJs) have been shown to encode sensory information in MLIs (16). MLIs are particularly interesting because their geometry is essentially restricted to a single parasagittal plane (17) and their biophysical properties are well characterized (18). Whereas in a 3D structure, slicing unavoidably damages some of the GJ coupling, the 2D MLI network is better preserved by slicing along the sagittal plane. This situation creates a unique opportunity to determine the network connectivity in a 2D structure, which is considerably easier to analyze than the usual 3D case.

In the present work we take advantage of the planar configuration of the MLI GJ-connected network to study its functional connectivity. Because the most common protein forming neuronal electrical synapses, Cx36, shows a strong expression in the brain during the two first postnatal weeks (19), we chose to work on juvenile rodents. Using this preparation we develop an approach for determining the number of neighbors immediately linked by GJs to a reference cell, as well as the functional "equivalent number of coupled cells" based on the total charge distributed in the electrically coupled network. We then investigate the implications of GJ connectivity in cellular computation. Finally, we show how this information can be used to build a constrained model of the GJ-connected network.

Results

Cx36 Mediates Electrical Coupling in Molecular Layer Interneurons. Morphological evidence indicates the presence of GJs between somas and dendrites of MLIs in adult rodents (11, 20). Functionally, electrical coupling has been described in adult guinea pig MLIs (6), but in young rats, electrical junctions have been reported to be weak and infrequent (21, 22). Connexin 36 and connexin 45 are the two main neuronal GJ proteins (1) and both have been found in the molecular layer of the cerebellum (19, 23, 24), suggesting their expression in MLIs. Even though MLIs express Cx45, normal GJs are maintained in $Cx45^{-/-}$ mice. By contrast, normal GJs cannot be detected in $Cx36^{-/-}$ mice (20), suggesting a role of Cx36 in electrical coupling between MLIs. We consequently examined electrical coupling in mice and rats and the involvement of Cx36 in this coupling.

First, we examined the presence of Cx36 in P13–14 rats with immunohistochemistry. We performed triple stainings with antibodies

Significance

Certain classes of central neurons, notably interneurons, are linked together by electrical synapses made by gap junctions, which play an important role in network function. Modeling electrically coupled interneuron networks has been limited by a lack of knowledge of the number of cells directly connected to a reference neuron and of the extent of charge redistribution in the network. We show that capacitive currents can be used to derive such information. We illustrate this method, using the network formed by cerebellar molecular layer interneurons. We establish a quantitative model of the network, and we estimate the influence of gap junctions on network excitability. The method may be generally applicable to sparsely electrically coupled networks, particularly if they are planar.

Author contributions: P.A. and A.M. designed research; P.A. performed research; P.A. and A.M. contributed new reagents/analytic tools; P.A. analyzed data; and P.A. and A.M. wrote the paper.

The authors declare no conflict of interest.

This article is a PNAS Direct Submission.

[1]To whom correspondence may be addressed. E-mail: ppalcami@hotmail.com or alain.marty@parisdescartes.fr.

targeting (*i*) Cx36, (*ii*) the calcium-binding protein parvalbumin (PV) that is expressed in some MLIs and in Purkinje cells, and (*iii*) the calcium-binding protein calbindin (CB) that is expressed only in Purkinje cells (n = 3 regions of interest per animal, n = 3 animals). Among MLIs, only cells in the inner molecular layer, mainly basket cells, express PV in P13–14 rats, because PV is developmentally regulated and is expressed at earlier stages in basket cells than in stellate cells (25). We found that Cx36 is expressed in the inner molecular layer and colocalizes with PV expressing MLIs (Fig. 1*A*). A total of 73 ± 6% of Cx36 immunolabeling colocalized with PV-positive immunolabeling whereas a smaller percentage of Cx36 puncta, 12 ± 6%, colocalized with CB-positive structures. The remaining Cx36 staining, 27 ± 6%, did not colocalize with PV and may be related to Cx36 expression in the dendrites of Golgi cells (12, 13) and on MLIs that do not express PV. Thus, the majority of Cx36 puncta in the inner molecular layer were located on PV-positive MLIs. Furthermore, Cx36 was often detected at crossings of MLI neurites, which are putative sites for electrical synapses (Fig. 1*A*).

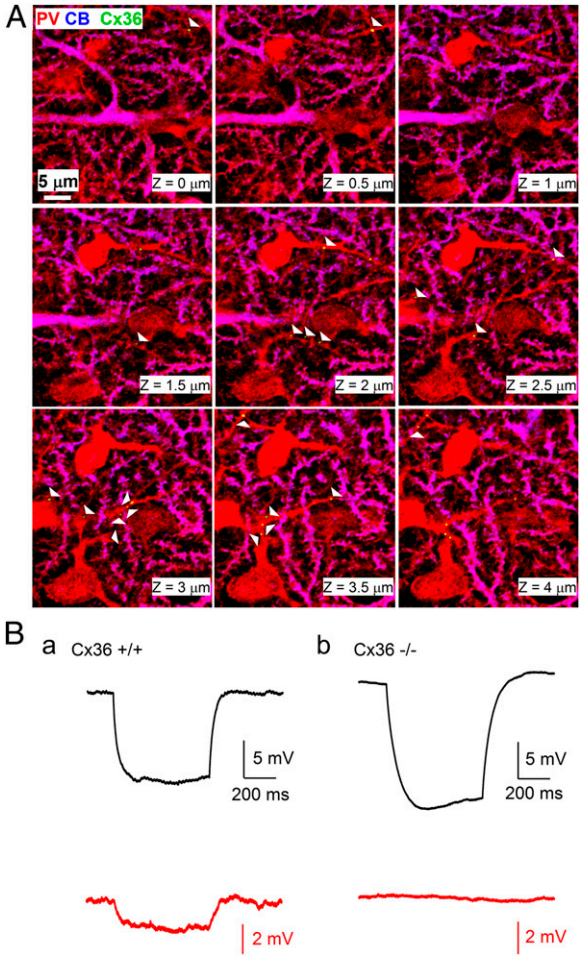

Fig. 1. Cx36 mediates electrical coupling between basket cells. (*A*) Cx36 is expressed at putative contacts between parvalbumin-positive MLIs. Shown is immunostaining for parvalbumin (PV, red), calbindin (CB, blue), and Cx36 (green), in cerebellar slices from juvenile rats. Successive confocal planes are shown. Arrowheads indicate Cx36 puncta, which are associated with PV^+, CB^- cells (presumably MLIs), and are mostly located at crossings between two PV^+, CB^- neurites. (*B*) Electrical coupling in control and $Cx36^{-/-}$ mice. Shown are whole-cell recordings from pairs of basket cells. Current pulses were injected in cell 1 (black) and the membrane potential was monitored in both the stimulated cell (black) and the other cell (red). Average of ~50 voltage traces is shown. (*a*) Representative recordings of pairs of basket cells from wild-type mice, showing steady-state coupling. (*b*) Representative recording of pairs of basket cells from $Cx36^{-/-}$ mice, showing no electrical connection.

Second, we examined electrical coupling in $Cx36^{-/-}$ mice (3). Electrical coupling was present in wild-type mice, where two-thirds of basket cell pairs with intersomatic distances smaller than 50 µm were coupled (n = 4/6 paired recordings, Fig. 1 *B*, *a*). In $Cx36^{-/-}$ mice, steady-state coupling was not detectable, and spikelets were not observed (n = 9 paired recordings, Fig. 1 *B*, *b*, Fisher's exact test on incidence of coupling, P = 0.01). These results confirm that Cx36 mediates electrical coupling between basket cells in young rodents.

Previous morphological studies showed that GJs were present in the somas and dendrites of MLIs (11, 20). Accordingly, we observed frequent Cx36 staining in MLI dendrites (Fig. 1*A*). Axonal GJs have been found in the basket axons around Purkinje cell bodies in a model of Purkinje cell degeneration (26). An open question is whether electrical synapses exist in the axons of normal rodent MLIs. We next looked for Cx36 in axonal structures. We observed Cx36 immunostainings that colocalized with MLI axons in 9 of 17 MLIs previously recorded with an internal solution containing neurobiotin (Fig. 2). The junctions were located in the main branch as well as in axonal collaterals. These experiments suggest that axonal GJs are present in nonpathological MLI axons and that they are not restricted to basket structures. Rather, they occur more generally in the axonal arborization of basket cells.

In summary, the presence of Cx36 in MLIs and the absence of electrical coupling in mice lacking Cx36 concur to indicate that Cx36 is the main molecular substrate of electrical synapses between MLIs.

Capacitive Currents in Basket Cells. GJs create a link between the capacitive compartments of neighboring cells and hence are expected to distribute capacitive currents in the electrically coupled network. This should be manifest in the analysis of capacitive currents under voltage clamp (27, 28). However, to our knowledge, a possible contribution of GJs to the capacitive current of mammalian INs has not been so far reported. We therefore reexamined capacitive currents in MLIs with the aim of identifying a possible contribution of GJs.

Juvenile MLIs have thick dendrites extending over a few tens of microns and a comparatively thin axon (diameter 0.6 µm) extending about 200 µm. Evidence gathered from experimental and modeling approaches indicates that dendrites are short enough to be considered as isopotential with the soma (18, 29). Passive electrical equilibration occurs between the axonal compartment and the somatodendritic compartment with a time constant of a few milliseconds (18). Under voltage clamp, when a hyperpolarizing voltage jump is applied to the soma of a MLI from young rat slices, capacitive currents display two distinct exponential components, reflecting the fast charge of the somatodendritic compartment and the slower charge of the axonal compartment (18). Likewise, compartmental modeling based on morphological reconstructions predicts a capacitive current trace that can be fitted by a biexponential curve with time constants τ_1 = 0.2 ms and τ_2 = 3.1 ms (18). This analysis was performed using pulses with a 20-ms duration, which ensured complete capacitive loading of both somatodendritic and axonal components.

However, if the duration of the pulses is extended beyond 20 ms, as in the present experiments, slower components become apparent in most cells (8/9). In Fig. 3 *A*, *b*, which shows a blow-up of the part of the relaxation boxed in red dashed lines in Fig. 3 *A*, *a*, a slow relaxation is apparent with a time constant of 14.5 ms. Once this slow component was removed by subtraction, the two previously described somatodendritic and axonal components were apparent (Fig. 3 *A*, *b* and *c*). We found in rat basket cells a first exponential term of amplitude A_1 = 702 ± 104 pA and time constant τ_1 = 0.40 ± 0.05 ms and a second term of amplitude A_2 = 145 ± 23 pA and time constant τ_2 = 3.0 ± 0.3 ms (n = 9, Fig. 3 *A*, *c*), close to previously reported values. The corresponding somatodendritic compartment (C_1 in Fig. 3 *A*, *d*) has a capacitance

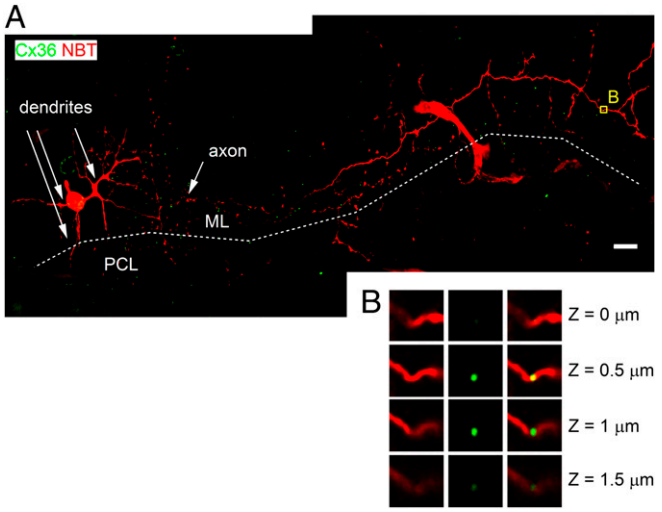

Fig. 2. Axonal location of Cx36 in some MLIs. (*A*) A basket cell filled with neurobiotin (red) and immunostained against Cx36 (green) displays a compact dendritic arborization and an extended axon running near the edge of the molecular layer (ML), parallel to the Purkinje cell layer (PCL; border between ML and PCL indicated by white line). Maximum of the Z projection from a stack of confocal planes is shown. (*B*) A magnification of the yellow box in *A* in four successive confocal planes shows a Cx36 cluster located in the main branch of the basket cell axon.

of 5.0 ± 0.2 pF and the axonal compartment (C_2 in Fig. 3 *A*, *d*) has a capacitance of 9.7 ± 2.5 pF.

The analysis indicated that additional exponential functions had to be included with amplitude A_3 = 42.1 ± 9.1 pA (averaged over 9 cells) and time constant τ_3 = 16.3 ± 1.9 ms (n = 8/9), accounting for 13.4 ± 3.2 pF. In 5 cells, a fourth time constant τ_4 = 100.6 ± 17.1 ms (n = 5/9) with average current amplitude over the entire population A_4 = 5.9 ± 2.1 pA (n = 9) accounts for 11.4 ± 4.1 pF (Fig. 3 *A*, *e*, n = 9). These slow components cannot be due to the contribution of the pipette capacitance because this contribution was removed by subtraction of cell-attached records (*Materials and Methods*), and they are not compatible with modeled charge time constants of dendritic or axonal compartments (18). Thus, whereas the somatodendritic and axonal compartments of rat basket cells have a summed capacitance of 14.7 ± 2.5 pF (n = 9), slower exponential components represent additional average capacitance values C_{3+4} = 24.8 ± 5.9 pF (n = 9).

In mouse basket cells, A_1 = 541 ± 71 pA, τ_1 = 0.33 ± 0.03 ms, A_2 = 135 ± 25 pA, τ_2 = 3.0 ± 0.7 ms, A_3 = 13.3 ± 1.4 pA, and τ_3 = 30.5 ± 5.0 ms (n = 5). Corresponding capacitances are C_1 = 3.5 ± 0.4 pF, C_2 = 6.9 ± 1.0 pF, and C_3 = 8.5 ± 2.0 pF (Fig. 3 *B*, *a* and *b*).

These results indicate that, in addition to somatodendritic and axonal capacitive currents, basket cells also display a slower capacitive current with a timescale of tens of milliseconds that loads a membrane surface similar to or larger than the cell's own surface.

Electrotonic Coupling Is Responsible for the Slow Capacitive Current in Basket Cells. Can electrical coupling explain the slow components of the capacitive current? In such a case C_3 + C_4 would represent the apparent membrane capacitance of one or several cells linked to the recorded cell by GJs (Fig. 3*C*; the exact representation of C_3 and C_4 in terms of cell membrane capacitance is discussed below in *Equivalent Number of Neighbors*).

In Cx36$^{-/-}$ mice, 10 of 11 basket cells displayed a third component with τ_3 = 8.7 ± 0.9 ms (n = 10), A_3 = 36.7 ± 7.6 pA (averaged over 11 cells). The third charge time constant τ_3 was significantly smaller in Cx36$^{-/-}$ mice than in wild-type mice (P = 0.0003, one-tailed Wilcoxon–Mann–Whitney two-sample rank test), reflecting the contribution of electrically coupled cells to it.

τ_3 values were so close to those of τ_2 in Cx36 $^{-/-}$ mice that the separation between the two components became questionable.

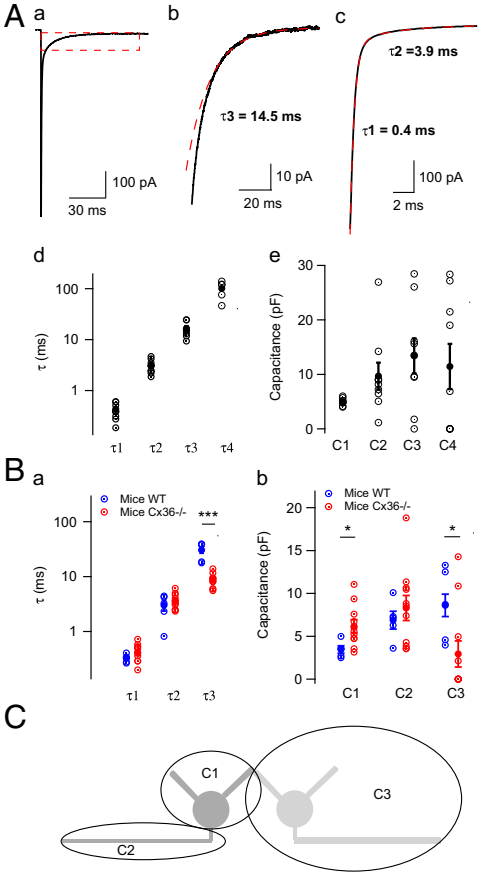

Fig. 3. Slow component of capacitive currents in basket cells reflects capacitive loading of neighboring cells through the GJ channel connexin 36. (*A*) Current relaxations evoked by a 50-mV voltage step in rat basket cells. (*a*) Capacitive current relaxation in a rat basket cell in response to a 50-mV hyperpolarizing jump in voltage-clamp mode (average of ~100 trials). (*b*) Enlargement of the red dashed box in *a*, showing the slow capacitive current (with time constant τ_3) present in 8/9 basket cells. In this example, τ_3 = 14.5 ms. A monoexponential fit (red) is superimposed to the original average trace (black). (*c*) The curve resulting from the subtraction of the slow component shown in *b* from the original data is fitted by a biexponential curve (red), with time constants τ_1 = 0.4 ms and τ_2 = 3.9 ms. (*d*) Time constants of the three exponential functions that fit the average current trace: τ_1, τ_2, and τ_3 (*n* = 8/9) and τ_4 (*n* = 5/9). (*e*) Capacitance of the corresponding three compartments. (*B*) Size and charging time constants of successive capacitance current components in mice basket cells. (*a*) Time constants of the three exponential functions that fit the average current trace in wild-type mice (blue) and in Cx36$^{-/-}$ mice (red). The value of τ_3 is significantly smaller in Cx36$^{-/-}$ mice than in control mice. τ_1 and τ_2 are not significantly different between wild-type mice and Cx36$^{-/-}$ mice. (*b*) Capacitance of the corresponding three compartments of basket cells in wild-type mice (blue) and Cx36$^{-/-}$ mice (red). Red symbols display means and associated SEM values. The capacitance of the first compartment (C_1) is significantly larger in MLIs from Cx36$^{-/-}$ mice than in those from wild-type mice. The capacitance of the second compartment (C_2) is not significantly different in Cx36$^{-/-}$ compared with wild-type mice. The capacitance of the third compartment (C_3) is significantly reduced in Cx36$^{-/-}$ mice. (*C*) Diagram of the three capacitive compartments of MLIs. Shown is a schematic representation of the three compartments deduced from current relaxations. C_1 and C_2 respectively represent the somatodendritic and the axonal compartment of the recorded cell. C_3 represents one or several cells linked to the recorded cell by electrical junctions.

Given our criteria for separation among successive exponential components (*Materials and Methods*), in 7 of 11 cells the third component was aggregated to the second one, leading to assigning a value of 0 to C_3. On average we found a value markedly smaller than in wild type (2.9 ± 1.5 pF vs. 8.5 ± 2.0 pF, P = 0.02, one-tailed Wilcoxon–Mann–Whitney two-sample test). This indicated that the third component is essentially due to the charge of the electrically coupled cells (Fig. 3*B*, *b*). The somatodendritic compartment had a somewhat larger capacitance in $Cx36^{-/-}$ than in wild-type mice (6.2 ± 0.7 pF vs. 3.5 ± 0.4 pF, P = 0.02, Wilcoxon–Mann–Whitney two-sample test), which may reflect compensatory mechanisms in dendritic morphology as shown in other preparations (30), whereas the capacitance of the axonal compartment did not show any difference between wild-type and $Cx36^{-/-}$ mice (P = 0.58, Wilcoxon–Mann–Whitney two-sample test). The other parameters obtained in $Cx36^{-/-}$ mice were A_1 = 790 ± 73 pA, τ_1 = 0.41 ± 0.05 ms and A_2 = 112 ± 15 pA, τ_2 = 3.7 ± 0.4 ms. P values for the comparison of the somatodendritic and axonal time constants τ_1 and τ_2 were, respectively, 0.26 and 0.51 (Wilcoxon–Mann–Withney two-sample rank test), confirming that these components do not reflect loading of coupled cells (Fig. 3*B*).

Thus, a distinct slow relaxation is absent in $Cx36^{-/-}$ mice, and the third slow capacitive component mostly reflects loading of coupled cells.

Equivalent Number of Neighbors. To derive a functional interpretation of GJs it is essential to know to which extent a voltage excursion is transmitted from a driver cell to the rest of the network. For this purpose we define the equivalent number of neighbors, N_{eq}, as

$$N_{eq} = \Sigma \Delta V_i / V_1, \quad [1]$$

where ΔV_i is the voltage deflection in cell i (i > 1), and 1 refers to the cell in which the voltage step is applied. N_{eq} is the sum of coupling coefficients over the entire network. Each cell contributes to the sum with a weight reflecting the proportion of the driving voltage that is transmitted to it. This sum has been recognized as critical for modeling the network connectivity (7).

Capacitive current analysis readily provides an estimate of N_{eq}. The equivalent capacitance corresponding to N_{eq} is

$$C_{eq} = C\ N_{eq} = C\Sigma\Delta V_i / \Delta V_1, \quad [2]$$

where C is the mean capacitance of a single cell (including the somatodendritic and axonal components). C_{eq} is the ratio between the capacitive charge distributed over the network and the driving potential. This ratio has been evaluated above as

$$C_{eq} \sim C_3 + C_4 = (A_3\ \tau_3 + A_4\ \tau_4)/\Delta V_1. \quad [3]$$

Combining Eqs. **2** and **3** leads to

$$N_{eq} \sim (A_3\ \tau_3 + A_4\ \tau_4)/(C\Delta V_1). \quad [4]$$

Numerical application in rat basket cells leads to C = 14.7 ± 2.5 pF (n = 7), C_{eq} = 24.8 ± 5.9 pF (n = 9), and N_{eq} = 1.69.

In conclusion, capacitive current analysis provides a direct estimate of N_{eq}. In addition, this analysis reveals an important difference between the first two components of input capacitance, C_1 and C_2, and the two last ones, C_3 and C_4. Whereas C_1 and C_2 each represent a specific membrane surface that is totally loaded to the driving potential, C_3 and C_4 represent membrane areas that are loaded to a fraction of the driving potential.

Electrical Junctions in Paired Current-Clamp Recordings. Next we examined electrical coupling among MLIs in a more standard manner, by performing double whole-cell recordings in MLIs from rats. To maximize coupling probability the distance between the two MLI somas was kept smaller than 40 μm, and the depth in the slice was matched within 10 μm such that the 2 MLIs were located at the same sagittal plane. In a first series of experiments we injected negative current pulses in one cell and compared the voltage changes measured in both cells under current clamp (Fig. 4*A*, *a*). These experiments revealed bidirectional electrical coupling in 29% of pairs (20 of 69 pairs; Fig. 4*A*, *b*). The average steady-state coupling coefficient measured at the end of the pulse was 15.4 ± 2.5% (n = 38 one-direction observations, detection threshold = 1%, Fig. 4*A*, *c*).

In all double recordings in which coupling was detected, action potentials in one cell evoked spikelets in the other (Fig. 4*B*, *a*). Spikelets result from filtering of the initial spike waveform by the combination of GJ resistance and postsynaptic cell capacitance (31). The average spikelet amplitude was 0.82 ± 0.09 mV (n = 38 observations, detection threshold ~0.1 mV, Fig. 4 *B*, *b*). In pairs that did not exhibit coupling, spikelets evoked by spikes in the other cell were not observed (Fig. 4*C*).

Respective time courses of spikes and spikelets can be seen in Fig. 4*B*, *a*. The delay between the rising phases of spike and spikelet, measured at half-maximal amplitude, was 0.93 ± 0.14 ms (n = 17 one-direction connections). Spikelet decay was biphasic, with a time constant of the initial decay phase of 5.6 ± 0.7 ms (membrane potential ~ −75 mV). This value is smaller than the membrane time constant (18). In MLIs, it has been shown that loading of the axonal membrane capacitance increases the initial decay rate of excitatory postsynaptic potentials (EPSPs) over the value predicted from the RC product of the cell membrane ("axonal speeding," ref. 18). Axonal speeding likely accelerates the decay of spikelets like it does for EPSPs.

Electrical coupling was also observed in experiments using whole-cell recording from one MLI (follower cell) and cell-attached recording from another MLI (driving cell). In this configuration, we found 11 coupled pairs from 19 recordings. Putting together double whole-cell and mixed whole-cell/cell-attached experiments, electrical coupling was observed in 35% of recorded pairs (31 of 88 pairs), close to 40% of that previously reported in adult guinea pigs (6).

The distributions of both coupling coefficients and spikelet amplitudes measured in paired whole-cell recordings are asymmetric, with a mode smaller than the mean and a tail of high values (Fig. 4 *A*, *c* and *B*, *b*). The two parameters were strongly correlated (P = 8×10^{-9}, linear correlation test, Fig. 4*D*).

Because the mean spikelet amplitude is 0.82 mV, and the average spike is 58 ± 1 mV (for basket cells, *n* = 30), as measured in whole-cell recordings, suprathreshold coupling takes the mean value of ~1.4%, i.e., one order of magnitude smaller than the steady-state coupling coefficient (15.4%). Thus, MLI electrical synapses transmit slow subthreshold events much more efficiently than spikes, as described in other preparations (31).

The coupling coefficient measured in one direction was as a rule different from that measured in the other direction. In 15 pairs, we measured the mean ratio between the two values of 1.7 ± 0.4 (n = 15). This does not necessarily imply a rectification of the GJ conductance, however. A similar apparent rectification has been reported earlier under current clamp in guinea pig MLIs, where it was shown to reflect differences in cellular resistances between the two recorded cells (6). Several lines of evidence indicate that the same applies here.

First, the ratio of coupling coefficients and the ratio of input resistances are strongly correlated (linear correlation test, P = 0.001, correlation coefficient r = 0.73, n = 15). Second, the directional junctional conductance can be estimated from paired current-clamp recordings by a two-cell approximation (6) as $G_{1\ to\ 2} = (\Delta V_2/\Delta V_1)/R_2[1 - (\Delta V_2/\Delta V_1)]$, where 1 and 2 are two coupled cells (Fig. 5*B*), ΔV_2 is the voltage deflection in cell 2 after a voltage step ΔV_1 is evoked in cell 1, and R_2 is the measured input resistance of cell 2. As shown in Fig. 5*B*, $G_{1\ to\ 2}$ and $G_{2\ to\ 1}$ take similar values, indicating no rectification. The residual conductance asymmetry apparent in Fig. 5*B* may be due to an asymmetry of leak conductance through the seal, which may

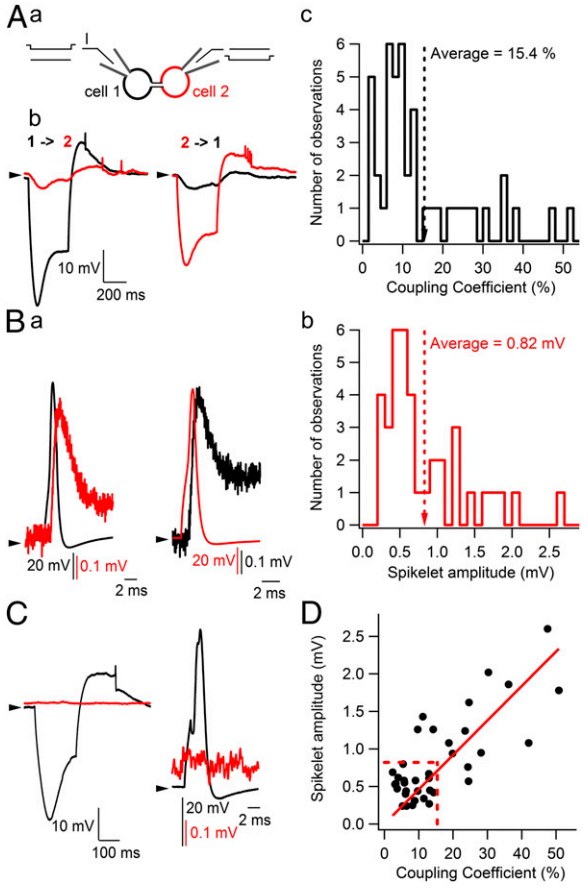

Fig. 4. Electrical coupling between MLIs. (*A*) Steady-state coupling. (*a*) Diagram of the experiment. Whole-cell recordings from pairs of neurons are shown. Current pulses were injected in one cell while a constant current was applied to the other. (*b*) (*Left*) Negative current step injected in cell 1. Average of ~20 traces is shown. Arrowhead: −70 mV. (*Right*) Negative current step injected in cell 2. Averages of ~20 traces are shown. Arrowhead: −70 mV. Cell 1 traces are black and cell 2 traces are red. In both *a* and *b* note the sag due to I_h current activation. Steady-state potential was measured at the end of the pulse, after the I_h sag. (*c*) Histogram of coupling coefficients measured in paired recordings as the ratio between the steady-state voltage change in one cell and the steady-state voltage change in the coupled cell. Note the non-Gaussian distribution, with a mode followed by a tail of large values. (*B*) Phasic coupling. Strong (2-ms duration) short current injection in one cell elicited a spike in that cell and a postsynaptic potential (spikelet) in the other. (*a*) (*Left*) The red trace illustrates average membrane potential of cell 2 triggered by spikes in cell 1 (black). Average of 20 traces is shown. (*Right*) Averages of the first cell membrane potential (black) triggered by spikes in cell 2 (red). Arrowhead: −70 mV. (*b*) Histogram of spikelet amplitudes. As in *A*, note the non-Gaussian distribution, with a mode followed by a tail of large values. (*C*) Example of a nonconnected pair. (*Left*) In response to a hyperpolarizing current jump in one cell, no steady-state coupling is observed in the other. (*Right*) Spikes in one cell fail to evoke spikelets in the other. Arrowhead: −70 mV. (*D*) Spikelet amplitude as a function of coupling coefficient. Spikelet amplitudes are tightly correlated to corresponding coupling coefficients. Dashed red lines, average values of the two parameters. The data are approximated with a line passing through the axes origin, with a slope of 0.46 mV for 10% coupling coefficient (solid red line).

significantly alter the estimate of the input resistance R in large resistance neurons, or to other measurement errors. Third, direct GJ conductance measurement under voltage clamp, described below, does not indicate rectification.

Overall, in a short spatial range ($d \leq 40$ μm), electrical synapses between MLIs in young rats are frequent, strong, and particularly efficient in transmitting slow subthreshold events. GABAergic transmission was observed in 11% of one-direction connections (17 of 157 one-direction connections) compared with electrical coupling, observed in 31 of 88 pairs (35%). Thus,

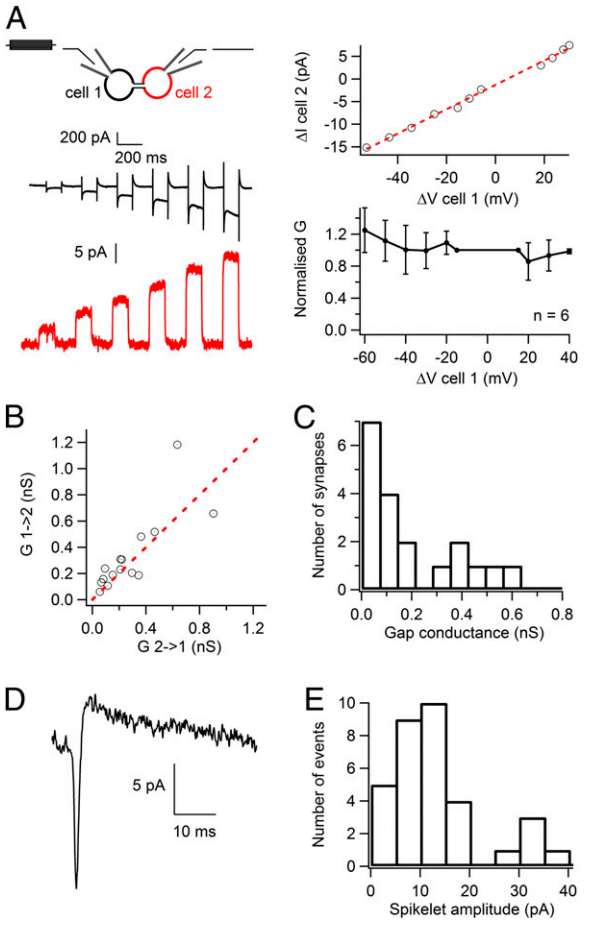

Fig. 5. Conductance and rectification of electrical synapses between MLIs. (*A*) Coupling conductance and lack of rectification of electrical coupling in voltage-clamp experiments. (*Left*) Experimental design and sample traces. Two electrically coupled cells were recorded under voltage clamp (holding potential −62 mV). When cell 1 was hyperpolarized, an inward current was evoked in cell 1 (black). The electrode of cell 2 delivered current (red) to maintain the potential of cell 2 to −62 mV. This current flowed through the GJ from cell 2 to cell 1, and its direction with respect to the amplifier clamping cell 2 was the same as that of depolarizing currents, i.e., outward. Depolarizing cell 1 had the inverse effect. The junctional conductance was then calculated as the ratio of the current change in cell 2 (ΔI_2) over the voltage change in cell 1 (ΔV_1). (*Upper Right*) Linear relationship between ΔI_2 and ΔV_1. A linear fit is superimposed on the experimental data, indicating a lack of voltage dependence of the gap conductance (G_{GAP} = 269 pS). Voltage-clamp errors due to the recording pipette resistance in cell 1 have been corrected. (*Lower Right*) Junctional conductance normalized to values obtained for ΔV_1 excursions between −15 mV and +15 mV. Pooled data for six pairs are shown. Mean ± SD shows no significant rectification. (*B*) Lack of rectification of electrical coupling in current-clamp experiments. Shown is coupling conductance measurement in electrically coupled pairs from current injections in both directions (from cell 1 to cell 2, $G_{1->2}$ and from cell 2 to cell 1, $G_{2->1}$). A line (y = x) is superimposed on the experimental data. (*C*) Histogram of coupling conductances. Shown is a histogram of junctional conductances (*n* = 19 pairs) measured in coupled cells. Mean = 190 pS. (*D*) Spikelet under voltage clamp. In many voltage-clamp recordings, moderate depolarization elicited spikelets that presumably reflected the firing of an electrically coupled neighboring cell following the spread of depolarization through the GJ. Average of 46 traces is shown. (*E*) Histogram of spikelet amplitudes. Summary data from 33 MLIs are shown. Mean = 13 pA.

at short spatial scales, electrical synapses are about three times more frequent than chemical synapses.

Electrical Junctions in Paired Voltage-Clamp Recordings. Voltage-clamp experiments were used to measure junctional conductance between the somas of two coupled cells (Fig. 5*A*). The junctional conductance was then calculated as the ratio of the current change ΔI in cell 2 over the voltage jump amplitude ΔV in cell 1. This gave a mean of 190 ± 43 pS (n = 19 MLIs, detection threshold ~10 pS). Values of GJ conductances gathered across various voltage-clamp experiments displayed a skewed distribution (Fig. 5*C*). The same experiments were used to examine possible rectifying properties of the GJs. We found no rectification at physiological subthreshold membrane potentials (Fig. 5*A*), confirming that the rectification observed under current clamp (see above) reflects differences in the input resistance values of the recorded cells.

When recording from a single cell under voltage clamp, slight depolarization often elicited a sequence of inward–outward currents (Fig. 5*D*). These signals are the counterparts of the spikelets described above under current-clamp conditions (Fig. 4*B*). Like the latter signals, they presumably reflect the firing of a cell that is electrically coupled to the recorded cell and that fires due to the spread of depolarization. Peak amplitudes of spikelet currents measured under voltage clamp had again a skewed distribution (Fig. 5*E*), consistent with the previous results on the strength of GJs.

Estimate of First-Order Electrically Coupled Neighbors. As pointed out before, current methods of GJ analysis do not readily distinguish direct neighbors from indirect neighbors. Here we take another approach, combining capacitive current analysis and paired recording data to estimate the number of direct electrically coupled neighbors, N_1. The initial amplitude of the slow components of the capacitive current, $A_3 + A_4$, corresponds to the current flowing into coupled cells through junctional conductances before changing the potential of these cells, at a point in time when the entire amplitude of the driving potential is applied across the GJs. Thus, the sum of the junctional conductances connecting the recorded cell to its direct electrically coupled neighbors is given by $G_{sum} = (A_3 + A_4)/\Delta V$. With ΔV = 50 mV, and after applying appropriate corrections (*Materials and Methods*), we obtain I_{sum} = [48.7–55.4] pA (n = 9) and G_{sum} = [974–1,108] pS.

Let G_{GAP} be the average junctional conductance between two basket cells. We can estimate the average number of directly connected cells N_1 as

$$N_1 = G_{sum}/G_{GAP} = (A_3 + A_4)/(\Delta V\, G_{GAP}). \quad [5]$$

As discussed above, G_{GAP} can be estimated with two different methods. A first estimate of G_{GAP} comes from the distribution of Fig. 5*C*, which has a mean value of 210 pS for basket cell pairs. We made a second estimate from the cells in which we measured spikelets in voltage clamp. Assuming a 58-mV excursion for the action potential in the neighboring basket cell (n = 30), applying Ohm's law to the GJ resistor leads to an estimate of 221 pS for basket cells. Unlike steady-state measurements, spikelets are fast signals that mostly arise across direct GJs. Entering the last G_{GAP} estimate into Eq. **5** yields N_1 = [4.4–5.0] cells for rat basket cells.

Difference in Cx36-Mediated Coupling Between Basket and Stellate Cells. Basket and stellate cells differ in their morphology, in their position in the molecular layer, and in the region of Purkinje cells that they target. In adult guinea pigs, dye coupling was found more frequently between stellate cells than between basket cells (6), but it remains unclear how general this result is across species and development stages.

We found that the expression of Cx36 was higher in the inner molecular layer than in the outer molecular layer in young rats (Fig. 6*A*, *a*). Eighty-eight percent of Cx36 puncta were located in the inner third of the molecular layer (Fig. 6*B*, *a*). The distribution of Cx36 puncta suggests a higher expression of Cx36 in basket cells than in stellate cells (whose somas are located in the inner third and in the two outer thirds of the molecular layer, respectively).

To test whether juvenile basket cells express more Cx36 puncta than stellate cells, we performed immunostainings against Cx36 on cells that had been previously filled with neurobiotin included in the patch pipette (Fig. 6*B*). Cx36 puncta were found in a small proportion of neurobiotin-filled stellate cells (n = 2/8), but in a large proportion of basket cells (n = 8/9). These had on average 2.5 Cx36 puncta (n = 8), whereas the two Cx36-expressing stellate cells expressed a single Cx36 cluster each. Note that, because of the limited antibody penetration in slices used for electrophysiology, these numbers are expected to be an underestimate of the total number of Cx36 puncta per cell.

We also found from our paired recordings performed at short (40 μm) distances in juvenile rats that the electrical coupling

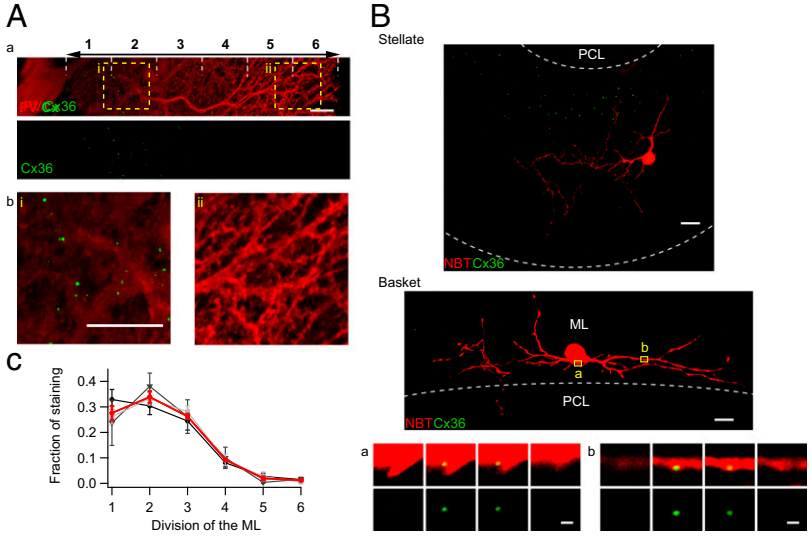

Fig. 6. Different levels of Cx36 expression in basket and stellate cells. (*A*) Gradient of expression of Cx36 in the molecular layer. An antibody targeting the protein parvalbumin (PV) was used to visualize the extent of the molecular layer in young rats (PN 13–14). (Scale bar, 10 μm.) (*a*) The majority of Cx36 puncta are located in the inner half of the molecular layer, whereas the outer half displays little Cx36 expression. (*b*) Enlargement of boxes shown in *a*. (*c*) Quantification of Cx36 gradient along the molecular layer. Stacks of 5-μm thickness were Z projected (maximum projection). The density of Cx36 puncta was quantified in six divisions of the molecular layer as illustrated in *a*. Three confocal acquisitions of 143 × 143 μm in different regions of the slice were taken for each of three perfused animals. Means of each animal are in gray or black, and mean among animals is in red. (*B*) Representative examples of single cells injected with neurobiotin. Maximum Z projection is shown of a stellate cell (*Upper*) and a basket cell (*Lower*) from a stack of confocal planes. No Cx36 was detected in the stellate cell shown; two puncta are shown in a basket cell soma and dendrite. (Scale bar, 10 μm.) ML, molecular layer; PCL, Purkinje cell layer. (*a* and *b*) Enlarged views from two regions (boxes *a* and *b*), showing in a sequence of adjacent horizontal planes (ΔZ = 0.5 μm) a close association of Cx36 staining with basket cell structure. (Scale bar, 1 μm.)

probability between basket cells (65%, n = 17/26) is about four times higher than that between either stellate–stellate connections (16%, n = 6/37) or mixed basket–stellate connections (20%, n = 1/5). Junctional conductance values are 210 ± 60 pS in basket cell to basket cell connections (n = 13 pairs) and 93 ± 41 pS in stellate cells (n = 3). Accordingly, we found that spikelet amplitudes were larger for basket cells (12.8 ± 1.8 pA, n = 20) than for stellate cells (5.9 ± 1.9 pA, n = 5, P = 0.012, Wilcoxon–Mann–Whitney two-sample test), leading to GJ conductance estimates of 221 pS and 116 pS for basket cells and stellate cells, respectively. Thus, from a functional point of view, GJs are more frequent and stronger among basket cells than among stellate cells.

A large difference also appears when considering the number of direct neighbors. A first estimate of G_{GAP} comes from the distribution of Fig. 5*B*, which has a mean value of 93 pS for stellate cell pairs. Spikelets in voltage clamp give values of 116 pS for stellate cells and spikes have amplitudes of 51 ± 4 mV (n = 7). In stellate cells, from capacitive relaxations we find A_1 = 683 ± 107 pA, τ_1 = 0.29 ± 0.06 ms; accounting for C_1 = 3.5 ± 0.6 pF, A_2 = 91.8 ± 10.6 pA, τ_2 = 2.46 ± 0.37 ms; accounting for C_2 = 4.6 ± 1.0 pF. In 3 out of 7 cells, we found a third compartment with A_3 = 6.3 ± 3.3 pA (averaged over n = 7) and τ_3 = 16.5 ± 4.8 ms (n = 3). The corrected value is A_3 = 7.0–7.8 pA (*Materials and Methods*). Thus, G_{sum} = 140–156 pS and N_1 = [1.2–1.3] cells (n = 7), whereas in basket cells, our previous estimates gave N_1 = [4.4–5.0] cells.

A large difference finally appears concerning N_{eq} estimates obtained from Eq. **4**. We found a value of 1.69 cells for rat basket cells as explained above. For juvenile rat stellate cells, applying Eq. **4** yields $N_{eq} = A_3\,\tau_3/(C\,\Delta V_1)$ = 0.23 cells, given that, C = 8.0 ± 1.3 pF, ΔV = 50 mV. This gives a ratio of 1.69/0.23 ~ 7 between the equivalent number of neighbors for basket cells and stellate cells.

Altogether, these results indicate that in juvenile rats, basket cells are more strongly connected by GJs than are stellate cells.

Junctional Conductances Are Major Determinants of Input Conductance. Electrical synapses contribute to the input conductance of neurons (7, 32, 33). Here we show that this contribution can be deduced from the capacitive current analysis. The average measured steady-state input conductance of rat basket cells was 269 ± 70 pS (n = 9). The corresponding cellular input resistance is R_{TOT} = 3.71 GΩ. This value is larger than measurements previously performed by us 20 ms after the voltage jump (1.65 GΩ in ref. 34) because it takes into account the slow components of capacitive current decay. Indeed, the average input resistance in the present study derived from current measurements at 20 ms was $R_{TOT\ (20ms)}$ = 1.59 GΩ (n = 9), in perfect agreement with our previous measurement.

The expression of the intrinsic resistance of a cell, R_L, follows the relation (7)

$$R_L = (\Sigma \Delta V_k)/I_1, \qquad [6]$$

where I_1 is the input current into the recorded cell, and k varies from 1 to infinity.

Because R_{TOT} is by definition

$$R_{TOT} = (\Delta V_1)/I_1, \qquad [7]$$

Eqs. **1**, **6**, and **7** may be combined together to give

$$R_L = (N_{eq} + 1)\ R_{TOT}. \qquad [8]$$

Entering the values of R_{TOT} (3.71 GΩ) and N_{eq} (1.69) in Eq. **8** gives R_L = 10.0 GΩ. In terms of conductances, G_L = 100 pS and G_{TOT} = 270 pS. Thus, the summed junctional conductances of a rat basket cell are responsible for 63% of cellular input conductance.

Accordingly, basket cells are expected to have smaller input conductances in $Cx36^{-/-}$ mice compared with wild-type mice. Experimental values were respectively 164 ± 43 pS (n = 7) and 532 ± 143 pS (n = 5), confirming that basket cells' input conductances are larger in wild-type than in $Cx36^{-/-}$ mice (one-tailed Wilcoxon–Mann–Whitney two-sample test, P = 0.002). These experiments confirm a major contribution of electrical coupling to the excitability of the network formed by MLIs.

Lattice Model of the Basket Cell Network. Based on the previous results the following model can be proposed for the basket cell network. We assume a square pattern where each cell is at the center of a square and is linked by direct GJs to each of the four cells located at the corners of the square (Fig. 7). This model is justified by (*i*) anatomical constraints, particularly the confinement of basket cells in one sagittal plane, and (*ii*) the estimated mean number of direct neighbors being close to four. In such a network the equivalent number of coupled neighbors can be estimated layer by layer. If r represents the coupling coefficient, a direct link to the first layer (blue cells in Fig. 7*A*) contributes N_1 r = 4 r. The second layer comprises four cells that are linked to two blue cells (yellow cells with large diameter in Fig. 7*A*), plus four cells that are linked to single blue cells (yellow cells with small diameter in Fig. 7*A*). Each doubly connected yellow cell contributes 2 r^2 to N_{eq}, and each singly connected yellow cell contributes r^2 to N_{eq}. Therefore, the total contribution of layer

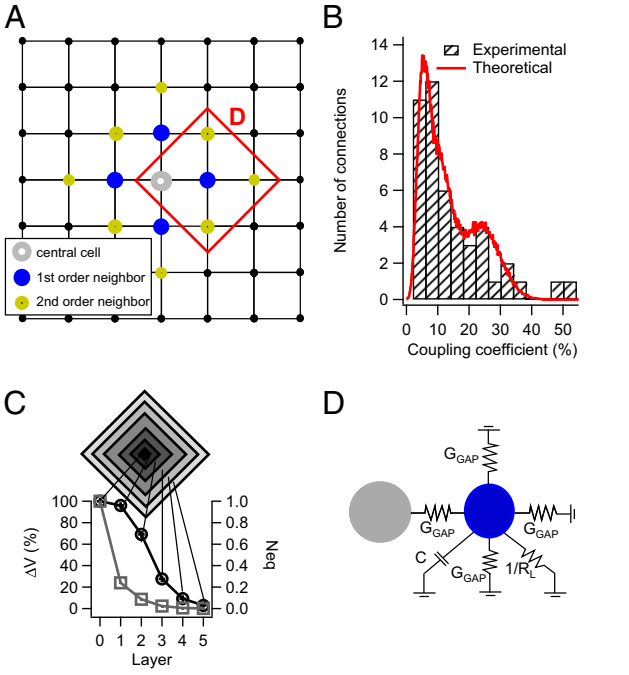

Fig. 7. Model of the electrically coupled basket cell network. (*A*) Square lattice representation of coupled cells. A central cell (gray) is surrounded by neighbors of the ith order organized in a square lattice. In accord with N_1 measurement, the central cell is connected to four first-order neighbors (blue), which are themselves connected to eight second-order neighbors (yellow). Some of the yellow cells are represented by larger circles because they are coupled to two first-order neighbors. (*B*) Distribution of coupling coefficients of first- and second-order connections. Shown is the distribution of coupling coefficients between basket cells and the theoretical distribution predicted from *A* (first- and second-order neighbors only). (*C*) Signal decay in successive coupled layers from a local perturbation in the square lattice. ΔV was computed for each layer of first-, second-, . . ., fifth-order neighbors in the square lattice, normalized to the value of ΔV in the central cell, for an average cell in each layer (squares) and for the sum of ΔV of all cells belonging to a given layer (circles). (*D*) Simplified model of the central cell and its electrically coupled neighbors. To model the capacitive current flowing into a first-order neighbor, the input conductance of this cell is approached by a combination of its links to its three other neighbors (through conductance G_{GAP}) plus its intrinsic input conductance $1/R_L$.

2 (yellow cells) is $8\,r^2 + 4\,r^2$. A similar reasoning can be made for subsequent layers, giving as a sum

$$\text{or } \begin{matrix} N_{eq} = 4\,r + (8+4)\,r^2 + (16+4)\,r^3 + \ldots \\ N_{eq} = \Sigma(8(j-1)+4)r^j, \end{matrix} \quad [9]$$

where j is the layer number ($j \geq 1$).

This calculation is only approximate because it neglects higher-order links (e.g., terms in r^3 and higher linking the central cell to the first layer). However, given the low value of the coupling coefficient this approximation is legitimate. Entering the mean experimental value for the coupling coefficient measured in paired current-clamp recordings ($r = 0.15$) in Eq. **9** yields $N_{eq} = 0.96$. This is somewhat smaller than our estimate $N_{eq} = 1.69$ obtained from the analysis of the capacitive currents. The discrepancy can easily be explained because the mean measured coupling coefficient is an underestimate of the value for direct links due to a proportion of indirect connections as discussed above. Eq. **9** can be inverted to calculate the value of r corresponding to $N_{eq} = 1.69$, giving a corrected coupling coefficient value of 0.24 for direct connections (calculation limited to the first two terms corresponding to C_3 and C_4). This limitation is in accord with our experiments, which do not make it possible to discriminate slower components.

According to the model of Fig. 7*A* the first and second layers carry most of the weight of N_{eq}, as illustrated in Fig. 7*C*. Together they account for 81% of N_{eq}. Neglecting higher-order layers, it is possible to estimate the distribution of coupling coefficients from the model of Fig. 7*A*. This calculation (*Materials and Methods*) assumes the sum of a Gaussian distribution of direct coupling values centered on 0.24, of a distribution of conductances for single indirect connections with 2 GJs in series (small yellow cells in Fig. 7*A*), and of another component representing doubly linked indirect connections (large yellow cells). The resulting curve constitutes a good approximation of the coupling coefficient distribution (Fig. 7*B*).

Despite the global extension of the network, local perturbations are not expected to propagate through the whole network, because coupling is relatively small. Following a step voltage deflection in the central cell, voltage deflections propagate to a few layers of the square lattice, as shown in Fig. 7*C* (squares, voltage at the individual cell level; circles, contribution of cell layer to N_{eq}).

Calculation of τ_3. As a test of the internal consistency of the above analysis, we compared calculated and experimental values for the slow component of the capacitive current, with time constant τ_3. An approximation can be made by simplifying the circuit of Fig. 7*A* as shown in Fig. 7*D*. The recorded cell is linked to each of its four neighbors by a conductance G_{GAP}. Each neighbor cell is represented by a combination of its capacitance C and of an equivalent conductance G. If voltage deflections in the yellow cells are neglected, G can be approximated to the combination of the cell membrane, with conductance $1/R_L$, and of three conductance pathways G_{GAP} corresponding to the three links to second-layer neighbors:

$$G = 1/R_L + 3\ G_{GAP}. \quad [10]$$

Given this approximation, the time constant of charge of the neighbor cell can be calculated as

$$\tau_3 = C/(G + G_{GAP}). \quad [11]$$

Eqs. **10** and **11** can be combined to yield

$$\tau_3 = C/(1/R_L + 4\ G_{GAP}). \quad [12]$$

Entering in this equation the rat basket cell experimental values $C = 14.7$ pF, $R_L = 10.0$ GΩ, and $G_{GAP} = 0.221$ nS, we obtain $\tau_3 = 14.9$ ms, compared with the experimental value $\tau_3 = 16.3$ ms. Thus, the model of Fig. 7*A*, with $N_1 = 4$, predicts a value for the time constant of the third capacitive current component that is close to experimental values. Another way to exploit this analysis is to offer an alternative estimate of N_1. The more general form of Eq. **12** is $\tau_3 = C/(1/R_L + N_1\ G_{GAP})$. Inversing this equation leads to $N_1 = 3.6$ cells, confirming that N_1 is close to 4.

Discussion

Local Capacitive Measurements to Deduce Network Topology. Two values have been previously discussed in the literature to estimate the size of electrically coupled assemblies: (*i*) the total number of directly or indirectly electrically coupled neighbors (M) and (*ii*) the number of directly connected neighbors (7) called here N_1. M was deduced from estimates of the probability of connectivity at various distances. However, obtaining a reliable estimate of M requires many paired recordings and is labor intensive. Concerning N_1, no direct estimate was available, and assumptions about the connectivity of the network were needed to deduce N_1 from M (7). In the present work we build a complete picture of the network by combining a quantitative analysis of the capacitive currents in single-cell recordings with measurements extracted from paired recordings.

A first benefit of capacitive current analysis is to provide a model-independent estimate of N_1, based on the measurement of the initial amplitude of the exponential current decay corresponding to the load of electrically coupled neighbors of the recorded cell. The comparison with the unitary conductance of electrical synapses provides a direct estimate of N_1. Because of the two-dimensional geometry of the MLI network, the connectivity of MLIs is unlikely to be significantly altered by slicing, so that this estimate applies in vivo as well. MLI results show that, at least as far as basket cells are concerned, most cells are electrically connected to the entire network. This analysis further allows us to deduce a network geometry from N_1, rather than using the previous approach of deducing N_1 from an a priori geometrical model.

We also use capacitive current analysis to introduce another functional parameter, N_{eq}, which represents the equivalent number of the cells loaded by the distribution of capacitive charges flowing from one cell. N_{eq} is a functional characterization of the membrane surface of coupled partners loaded by the redistribution of charges through GJs. $N_{eq} < M$, because each cell is weighted by the fraction of the voltage excursion that is transmitted from the driven cell. It represents the spread of a local perturbation. Our finding that N_{eq} is 1.69 for basket cells expresses that the computational unit in the basket cell network is not a single neuron, but a small cluster of $1 + 1.69 = 2.69$ electrically coupled neurons.

A potential limitation of the present approach is that it rests on the ability to separate the component of the capacitive current associated with electrical coupling, which has here a time constant in the order of tens of milliseconds, from the components reflecting the capacitive loading of the recorded cell. This separation is possible in juvenile MLIs, which have a well-characterized cellular biophysical compartmentalization with time constants below ~5 ms (18). The present method may likewise be of use in estimating the electrical connectivity of coupled networks formed by relatively compact cells with a small number of neighbors like pancreatic β-cells (35). It remains to be seen whether a similar separation can be obtained in other interneuron networks. On the one hand, intrinsic capacitive currents would be slower in neurons exhibiting more extended neuritic trees than MLIs. On the other hand, if the network is highly coupled, as typically expected for many 3D structures, the amplitude of the GJ-mediated capacitive currents will increase and their time constant will decrease (Eq. **12**). In either case the distinction between GJ-associated capacitive currents and intrinsic capacitive currents may be compromised. Finally, in the extreme case of a GJ-linked syncytium (36), as formed by glial cells, proper voltage control of the recorded cell becomes impossible. The input impedance being

dominated by the series resistance of the recording pipette, the amplitude of capacitive currents is severely reduced (36), making the capacitive current analysis impractical.

Functional Implications. The finding that the GJ-linked functional unit comprises (N_{eq} + 1) cells implies that the input capacitance and input conductance are multiplied by (N_{eq} + 1) compared with those of an isolated cell, a factor of ∼2.7 for rat basket cells. Therefore, GJs exert a very potent regulatory role on the network excitability, and they are expected to strongly modify responses to incoming synaptic inputs. The position of GJs between cells and their association with cell capacitance imply that this modulation depends on the spatial and temporal pattern of the synaptic input. The functional consequences of this modulation remain to be investigated. On the one hand, coupling may additionally average out noise generated at the cellular level by effectively dividing slow voltage fluctuations by a factor (N_{eq} + 1). On the other hand, electrical coupling propagates voltage fluctuations in coupled cells and could be the source of correlated subthreshold membrane potential fluctuations among neighboring MLIs.

We find that in young rodents, basket cells are more coupled locally than are stellate cells. The implications of these results for cerebellar processing remain to be investigated. In the temporal domain stellate cells may provide local, asynchronous signals, and basket cells may form more extended and coherent signals. In the spatial domain, basket cells may form larger electrically coupled assemblies and extend the spatial dimensions of inhibition to several Purkinje cells. Basket cells may also contribute to increase the strength of somatic inhibition and degree of synchrony by converging coupled MLIs to a single Purkinje cell.

Materials and Methods

Slice Preparation. All experimental procedures followed the animal care guidelines of Université Paris Descartes (approval no. A-750607), in agreement with European Directive 86/609/EEC. Sagittal slices (200 μm thick) were prepared from the cerebellar vermis of Sprague–Dawley rats [postnatal day (PN) 12–17] or C57BL/6J wild-type mice (PN 10–13) or $Cx36^{-/-}$ mice (PN 10–13). Rats or mice of either sex were decapitated before removal of the cerebellum. Cerebellar slices were made using a Leica VT 1000S vibratome while the cerebellum was bathed in an ice-cold artificial cerebrospinal fluid (ACSF) (composition 130 mM NaCl, 2.5 mM KCl, 26 mM $NaHCO_3$, 1.3 mM NaH_2PO_4, 10 mM glucose, 2 mM $CaCl_2$, and 1 mM $MgCl_2$; osmolarity 300 mosM) that was equilibrated with 95% (vol/vol) O_2 and 5% (vol/vol) CO_2 (pH 7.4). Slices were incubated for 40 min to 1 h at 34 °C in oxygenated ACSF and kept at room temperature for not longer than 7 h. $Cx36^{-/-}$ mice were kindly provided by H. Monyer, Department of Clinical Neurobiology, Heidelberg University Medical Center, Heidelberg (3).

Electrophysiology. Procedures to record from MLIs were as described in ref. 37. Slice regions were selected for recording where cell density was at least five cells per 100 μm^2 in the uppermost 20-μm-deep slice tissue, as visualized with differential interference contrast microscopy. INs taken from the internal third of the molecular layer were considered basket cells, and INs taken from the external two-thirds were considered stellate cells.

Whole-Cell Recordings. The standard internal recording solution contained 144 mM K gluconate, 6 mM KCl, 4.6 mM $MgCl_2$, 2 mM $CaCl_2$, 1 mM EGTA, 10 mM Hepes, 0.4 mM Na_2GTP, 4 mM Na_2ATP, pH 7.4; osmolarity, 295 mosM. The total Cl^- concentration in this solution (15.2 mM) was in accordance to the internal Cl^- concentration derived from reversal potential determinations with gramicidin perforated patch recordings (38). Whole-cell recording pipettes containing the K gluconate solution had an open tip resistance from 7 MΩ to 10 MΩ. Junction potentials were taken into account in the presentation of whole-cell recording data (12 mV were subtracted from the values read from the amplifier). Series resistance was not compensated. Experiments with leaky recordings (< −50 pA at −60 mV) were rejected.

In most experiments, the $GABA_A$ receptor blocker gabazine (SR-95531; 10–30 μM) was used. However, when effects of chemical synapses were irrelevant (e.g., in measurements of GJ properties with paired recordings), data with and without gabazine were pooled together.

Current Relaxations in Response to a Hyperpolarizing Voltage Step. We measured capacitive currents in voltage-clamp mode by examining the current relaxations to the steady state in response to square hyperpolarizing voltage steps. At hyperpolarized potentials the main time-dependent conductance is mediated by I_h channels (39). To minimize the contribution of I_h currents to slow capacitive currents, two alternative strategies were used. First, capacitive currents were recorded in the presence of the I_h blocker ZD-7288 at 30 μM. In these experiments voltage steps of −20 mV to −50 mV were applied from a holding membrane potential of ∼ −70 mV. Alternatively, capacitive currents were measured in cells held at ∼ −50 mV, and 20 mV hyperpolarizing voltage steps were performed in a voltage range in which I_h activation is small or absent and does not overlap with passive capacitive relaxations. The results obtained with the two protocols were similar and the results were pooled together.

Capacitive currents in MLIs display time constants ranging over more than two orders of magnitude. To separate the various components the following procedure was adopted. To determine slow components (time constants τ_3 and τ_4), a biexponential fit of the capacitive current was performed starting 20 ms after the beginning of the voltage jump to the steady state. When the ratio between the two time constants of the fit was smaller than 3.5, the fit was rejected and a single exponential fit, with a single time constant τ_3, was used instead. Then, to determine fast components (time constants τ_1 and τ_2), the fit of the slow component(s) was subtracted from the current trace and a new biexponential fit was performed to the subtracted curve over the first 20 ms of the current relaxation ("peeling procedure"). In the case where the ratio between τ_2 and τ_3 was less than 3.5, we assumed slow components to be absent and we did not subtract the monoexponential fit from the original trace before performing a biexponential fit on the first 20 ms of the trace. The choice of 3.5 as the cutoff ratio was guided by (*i*) previous practice (18) and (*ii*) empirical evaluation of our ability to disambiguate dual exponential components as a function of their time constant ratio.

The integral of an exponential is obtained by multiplying its initial amplitude by its decay time constant. The capacitance of each component represented by an exponential term $Ae^{-t/\tau}$, with amplitude A and time constant τ, was therefore calculated as $C = A\tau/\Delta V$, where ΔV is the voltage deflection. This equation is applicable only to the extent that the potential across the capacitor C is equal to the command potential ΔV. This is an acceptable approximation for the first two components of the capacitive currents, called C_1 (somatodendritic) and C_2 (axonal) hereafter. For the slower components C_3 and C_4, differences between command and local potentials are substantial and need to be corrected for; C3 and C4 represent membrane areas loaded to a fraction of the driving potential.

An error arises for A_3 and A_4 at the beginning of the relaxations. Because the loading of the intrinsic capacitance component and the capacitance linked to the electrically coupled cells is sequential, the local potential for one component rises with a speed matching that of the charge of the previous component. For this reason, the actual value of the instantaneous current A_3 is overevaluated by a factor close to τ_1/τ_3 in the case of somatodendritic gap junctions and of τ_2/τ_3 in the case of axonal gap junctions. Finally a correction needs to be applied to account for the steady-state current flowing along GJs, leading to an additive factor $I_{steady\ state} \times [N_{eq}/(1 + N_{eq})]$, with N_{eq} being approximated by Eq. **1**. In the case of a somatodendritic gap junction, the corrected instantaneous current I_{sum} can be estimated as $I_{sum} = A_3 (1 - \tau_1/\tau_3) + A_4 + I_{steady\ state} \times [N_{eq}/(1 + N_{eq})]$. In the case of an axonal gap junction, $I_{sum} = A_3 (1 - \tau_2/\tau_3) + A_4 + I_{steady\ state} \times [N_{eq}/(1 + N_{eq})]$.

Intracellular Tracer. Intracellular dye filling was performed by including in the internal solution 0.25–1% neurobiotin. Neurobiotin was revealed for 3 h at room temperature with rhodamine-conjugated streptavidin red (1:200; Jackson) or Alexa 488-coupled streptavidin (1:300; Invitrogen).

Immunostaining. PN 13–14 rats were intracardially perfused with 50 mL PBS (Sigma) followed by 50 mL of 4% paraformaldehyde (PFA) (Sigma). Cerebellar vermis was then postfixed for 1 h in 4% PFA at room temperature and then washed in PBS. All of the following procedures were performed at room temperature. Sagittal slices (40–50 μm thick) were permeabilized with 0.3% Triton for 30 min, washed three times with PBS, and incubated in 10% BSA (Sigma) for 20 min. The following primary antibodies were then incubated overnight: monoclonal mouse anti-Cx35/36 1:1,000 (Millipore; MAB3045), polyclonal rabbit anti-parvalbumin 1:1,000, and polyclonal guinea pig anti-calbindin 1:500 (Synaptic Systems). Secondary antibodies were coupled to anti-mouse Alexa 488 (Invitrogen Europe), anti-rabbit Alexa 546 (Invitrogen Europe), or anti-guinea pig Alexa 633, all used at 1:400 dilution. Immunostainings were also performed on acute slices (200 μm thick) with the same procedure, with the caveat that penetration was less effective than in thinner slices (40–50 μm) from

perfused animals. The specificity of the antibody against Cx36 has been previously tested in the molecular layer of $Cx36^{-/-}$ mice (13).

Confocal Imaging. Confocal acquisitions were performed on an LSM510 Zeiss microscope equipped with an argon laser (488 nm excitation), two helium–neon lasers (543 nm and 633 nm excitation), and a 63×/1.4 Plan-Apochromat objective. Successive planes were acquired at $\Delta z = 0.48$ μm and $\Delta x = \Delta y = 0.07$ μm. Image size was 2,048 × 2,048 pixels and typical acquisitions involved eight averages per plane.

Image Analysis. Images were analyzed with National Institutes of Health software ImageJ. Quantification of colocalization was performed on confocal stacks of 7,800 μm^3 in the inner molecular layer of three perfused animals. Brightness and contrast were adjusted, and threshold binarization was performed. Jacop plugin was used to assess colocalization, using Mander's coefficients. Cx36 puncta were determined using size, intensity, and circularity criteria (ImageJ plugin Particles Analysis). In experiments in which single cells were filled with neurobiotin, colocalization of Cx36 and neurobiotin was determined when Mander's coefficient was above 0.4.

Neurite Identity. The axon was identified as a thin neurite emerging from the soma or from one primary dendrite (17). The identification was confirmed by additional features, including the presence of basket terminals, the typical orthogonal branching pattern, the presence of varicosities, and neurite length well beyond dendritic extension.

Numerical Simulations. To perform numerical simulation of the coupling coefficient distribution, a realization of coupling coefficients between two direct neighbors (N_1) was generated from a Gaussian distribution (mean, 0.24; SD, 0.06). To generate a second Gaussian distribution corresponding to indirect neighbors (N_2), the data were shuffled and the resulting coupling coefficients were multiplied by those of the initial distribution. The distribution of indirect coefficients connected to two first-order neighbors (N_3) was generated by adding the values of two shuffled N_2 distributions. The distribution of all coupling coefficients of direct and indirect neighbors was generated by the sum of N_1, N_2, and N_3.

ACKNOWLEDGMENTS. We thank A. Jalil for valuable help in immunostaining experiments. We are grateful to Hannah Monyer for kindly providing $Cx36^{-/-}$ mice. We thank Philippe Ascher for his generous advice throughout this work and P. Ascher, J. Bao, T. Collin, J. Kehoe, J. Kim, I. Llano, C. Sotelo, and S. Tsuda for helpful suggestions on the manuscript. This work was supported by a PhD fellowship from Pierre et Marie Curie University (to P.A.), by the Centre National de la Recherche Scientifique (P.A.), and by Agence Nationale de la Recherche Grant Interneuron Network (to A.M.).

1. Galarreta M, Hestrin S (2001) Electrical synapses between GABA-releasing interneurons. *Nat Rev Neurosci* 2(6):425–433.
2. Tamás G, Buhl EH, Lörincz A, Somogyi P (2000) Proximally targeted GABAergic synapses and gap junctions synchronize cortical interneurons. *Nat Neurosci* 3(4):366–371.
3. Hormuzdi SG, et al. (2001) Impaired electrical signaling disrupts gamma frequency oscillations in connexin 36-deficient mice. *Neuron* 31(3):487–495.
4. Bartos M, et al. (2002) Fast synaptic inhibition promotes synchronized gamma oscillations in hippocampal interneuron networks. *Proc Natl Acad Sci USA* 99(20): 13222–13227.
5. Lewis TJ, Rinzel J (2003) Dynamics of spiking neurons connected by both inhibitory and electrical coupling. *J Comput Neurosci* 14(3):283–309.
6. Mann-Metzer P, Yarom Y (1999) Electrotonic coupling interacts with intrinsic properties to generate synchronized activity in cerebellar networks of inhibitory interneurons. *J Neurosci* 19(9):3298–3306.
7. Amitai Y, et al. (2002) The spatial dimensions of electrically coupled networks of interneurons in the neocortex. *J Neurosci* 22(10):4142–4152.
8. Calì C, et al. (2008) Inferring connection proximity in networks of electrically coupled cells by subthreshold frequency response analysis. *J Comput Neurosci* 24(3):330–345.
9. Mills SL, Massey SC (1998) The kinetics of tracer movement through homologous gap junctions in the rabbit retina. *Vis Neurosci* 15(4):765–777.
10. Hoge GJ, et al. (2011) The extent and strength of electrical coupling between inferior olivary neurons is heterogeneous. *J Neurophysiol* 105(3):1089–1101.
11. Sotelo C, Llinás R (1972) Specialized membrane junctions between neurons in the vertebrate cerebellar cortex. *J Cell Biol* 53(2):271–289.
12. Dugué GP, et al. (2009) Electrical coupling mediates tunable low-frequency oscillations and resonance in the cerebellar Golgi cell network. *Neuron* 61(1):126–139.
13. Vervaeke K, et al. (2010) Rapid desynchronization of an electrically coupled interneuron network with sparse excitatory synaptic input. *Neuron* 67(3):435–451.
14. Hull C, Regehr WG (2012) Identification of an inhibitory circuit that regulates cerebellar Golgi cell activity. *Neuron* 73(1):149–158.
15. Middleton SJ, et al. (2008) High-frequency network oscillations in cerebellar cortex. *Neuron* 58(5):763–774.
16. Chu CP, Bing YH, Liu H, Qiu DL (2012) Roles of molecular layer interneurons in sensory information processing in mouse cerebellar cortex Crus II in vivo. *PLoS ONE* 7(5): e37031.
17. Palay SL, Chan-Palay V (1974) *Cerebellar Cortex: Cytology and Organization* (Springer, Heidelberg).
18. Mejia-Gervacio S, et al. (2007) Axonal speeding: Shaping synaptic potentials in small neurons by the axonal membrane compartment. *Neuron* 53(6):843–855.
19. Condorelli DF, Trovato-Salinaro A, Mudò G, Mirone MB, Belluardo N (2003) Cellular expression of connexins in the rat brain: Neuronal localization, effects of kainate-induced seizures and expression in apoptotic neuronal cells. *Eur J Neurosci* 18(7): 1807–1827.
20. Van Der Giessen RS, Maxeiner S, French PJ, Willecke K, De Zeeuw CI (2006) Spatiotemporal distribution of Connexin45 in the olivocerebellar system. *J Comp Neurol* 495(2):173–184.
21. Vincent P, Marty A (1993) Neighboring cerebellar Purkinje cells communicate via retrograde inhibition of common presynaptic interneurons. *Neuron* 11(5):885–893.
22. Trigo FF, et al. (2010) Presynaptic miniature GABAergic currents in developing interneurons. *Neuron* 66(2):235–247.
23. Maxeiner S, et al. (2003) Spatiotemporal transcription of connexin45 during brain development results in neuronal expression in adult mice. *Neuroscience* 119(3): 689–700.
24. Helbig I, et al. (2010) *In vivo* evidence for the involvement of the carboxy terminal domain in assembling connexin 36 at the electrical synapse. *Mol Cell Neurosci* 45(1): 47–58.
25. Collin T, et al. (2005) Developmental changes in parvalbumin regulate presynaptic Ca2+ signaling. *J Neurosci* 25(1):96–107.
26. Sotelo C, Triller A (1979) Fate of presynaptic afferents to Purkinje cells in the adult nervous mutant mouse: A model to study presynaptic stabilization. *Brain Res* 175(1): 11–36.
27. Getting PA (1974) Modification of neuron properties by electrotonic synapses. I. Input resistance, time constant, and integration. *J Neurophysiol* 37(5):846–857.
28. Santos-Sacchi J (1991) Isolated supporting cells from the organ of Corti: Some whole cell electrical characteristics and estimates of gap junctional conductance. *Hear Res* 52(1):89–98.
29. Pouzat C, Marty A (1999) Somatic recording of GABAergic autoreceptor current in cerebellar stellate and basket cells. *J Neurosci* 19(5):1675–1690.
30. De Zeeuw CI, et al. (2003) Deformation of network connectivity in the inferior olive of connexin 36-deficient mice is compensated by morphological and electrophysiological changes at the single neuron level. *J Neurosci* 23(11):4700–4711.
31. Bennett MV, Zukin RS (2004) Electrical coupling and neuronal synchronization in the Mammalian brain. *Neuron* 41(4):495–511.
32. Bennett MV (1966) Physiology of electrotonic junctions. *Ann N Y Acad Sci* 137(2): 509–539.
33. Vervaeke K, Lorincz A, Nusser Z, Silver RA (2012) Gap junctions compensate for sublinear dendritic integration in an inhibitory network. *Science* 335(6076):1624–1628.
34. Alcami P, Franconville R, Llano I, Marty A (2012) Measuring the firing rate of high-resistance neurons with cell-attached recording. *J Neurosci* 32(9):3118–3130.
35. Benninger RK, Zhang M, Head WS, Satin LS, Piston DW (2008) Gap junction coupling and calcium waves in the pancreatic islet. *Biophys J* 95(11):5048–5061.
36. Maglione M, et al. (2010) Oligodendrocytes in mouse corpus callosum are coupled via gap junction channels formed by connexin47 and connexin32. *Glia* 58(9):1104–1117.
37. Llano I, Gerschenfeld HM (1993) Inhibitory synaptic currents in stellate cells of rat cerebellar slices. *J Physiol* 468:177–200.
38. Chavas J, Marty A (2003) Coexistence of excitatory and inhibitory GABA synapses in the cerebellar interneuron network. *J Neurosci* 23(6):2019–2031.
39. Mejia-Gervacio S, Marty A (2006) Control of interneurone firing pattern by axonal autoreceptors in the juvenile rat cerebellum. *J Physiol* 571(Pt 1):43–55.